Acta Crystallographica Section A
Foundations of Crystallography
ISSN 0108-7673

Received 5 May 2013
Accepted 2 September 2013

Comparative study of X-ray charge-density data on $CoSb_3$

Mette Stokkebro Schmøkel,[a] Lasse Bjerg,[a] Finn Krebs Larsen,[a] Jacob Overgaard,[a] Simone Cenedese,[b] Mogens Christensen,[a] Georg K. H. Madsen,[c] Carlo Gatti,[b] Eiji Nishibori,[d] Kunihisa Sugimoto,[e] Masaki Takata[d] and Bo Brummerstedt Iversen[a]*

[a]Center for Materials Crystallography, Department of Chemistry and iNANO, Aarhus University, Langelandsgade 140, DK-8000 Aarhus C, Denmark, [b]Istituto di Scienze e Tecnologie Molecolari del CNR (CNR–ISTM) e Dipartimento di Chimica, Università di Milano, via Golgi 19, I-20133, Milano, Italy, [c]Department of Atomistic Modelling and Simulation, ICAMS, Ruhr-Universität, Bochum, Germany, [d]RIKEN SPring8 Center, RIKEN, 1-1-1, Kouto, Sayo-cho, Sayo-gun, Hyogo 679-5148, Japan, and [e]Japan Synchrotron Radiation Research Institute I-I-I, Kouto, Sayo-cho, Sayo-gun, Hyogo 679-5198, Japan. Correspondence e-mail: bo@chem.au.dk

$CoSb_3$ is an example of a highly challenging case for experimental charge-density analysis due to the heavy elements (suitability factor of ~0.01), the perfect crystallinity and the high symmetry of the compound. It is part of a family of host–guest structures that are potential candidates for use as high-performance thermoelectric materials. Obtaining and analysing accurate charge densities of the undoped host structure potentially can improve the understanding of the thermoelectric properties of this family of materials. In a previous study, analysis of the electron density gave a picture of covalent Co–Sb and Sb–Sb interactions together with relatively low atomic charges based on state-of-the-art experimental and theoretical data. In the current study, several experimental X-ray diffraction data sets collected on the empty $CoSb_3$ framework are compared in order to probe the experimental requirements for obtaining data of high enough quality for charge-density analysis even in the case of very unsuitable crystals. Furthermore, the quality of the experimental structure factors is tested by comparison with theoretical structure factors obtained from periodic DFT calculations. The results clearly show that, in the current study, the data collected on high-intensity, high-energy synchrotron sources and very small crystals are superior to data collected at conventional sources, and in fact necessary for a meaningful charge-density study, primarily due to greatly diminished effects of extinction and absorption which are difficult to correct for with sufficient accuracy.

1. Introduction

$CoSb_3$ is a highly important host–guest material for the engineering of high-performance thermoelectric materials (Singh & Pickett, 1994; Morelli *et al.*, 1995). Its crystal structure has empty cavities and, when guest atoms are added to $CoSb_3$, its thermoelectric properties are greatly enhanced due to decreased thermal conductivity. Addition of guest atoms also provides control of the charge carrier concentration, which results in an increase in the thermoelectric power factor (Caillat *et al.*, 1996; Nolas *et al.*, 1996; Sales *et al.*, 1996; Anno *et al.*, 1999; Mi *et al.*, 2010, 2011). In order to understand the origin of the thermoelectric properties of this family of materials, it is important to understand the crystal structure and chemical bonding of the undoped host material (Caillat *et al.*, 1996; Sofo & Mahan, 1998; Nolas *et al.*, 1999; Bertini & Gatti, 2004; Chakoumakos & Sales, 2006). One way of achieving this is through analysis of the charge density (CD), which in principle can be obtained either from modelling of X-ray diffraction data, or from *ab initio* theoretical calculations.

A few years ago an X-ray charge-density study of $CoSb_3$ was published (Ohno *et al.*, 2007) based on low-temperature (10 K), short-wavelength (0.42 Å) and high-resolution (d_{min} = 0.33 Å) synchrotron powder diffraction data measured at SPring8, Japan. The maximum entropy method (MEM) was used to determine the thermally smeared experimental CD and a simple bond analysis was carried out (*e.g.* comparison of thermally smeared electron-density values in bond midpoints). In order to extend that study, we recently communicated a proper topological description of the $CoSb_3$ CD (Schmøkel *et al.*, 2013) based on analysis of state-of-the-art single-crystal synchrotron X-ray diffraction data collected at SPring8 combined with accurate theoretical calculations. In that

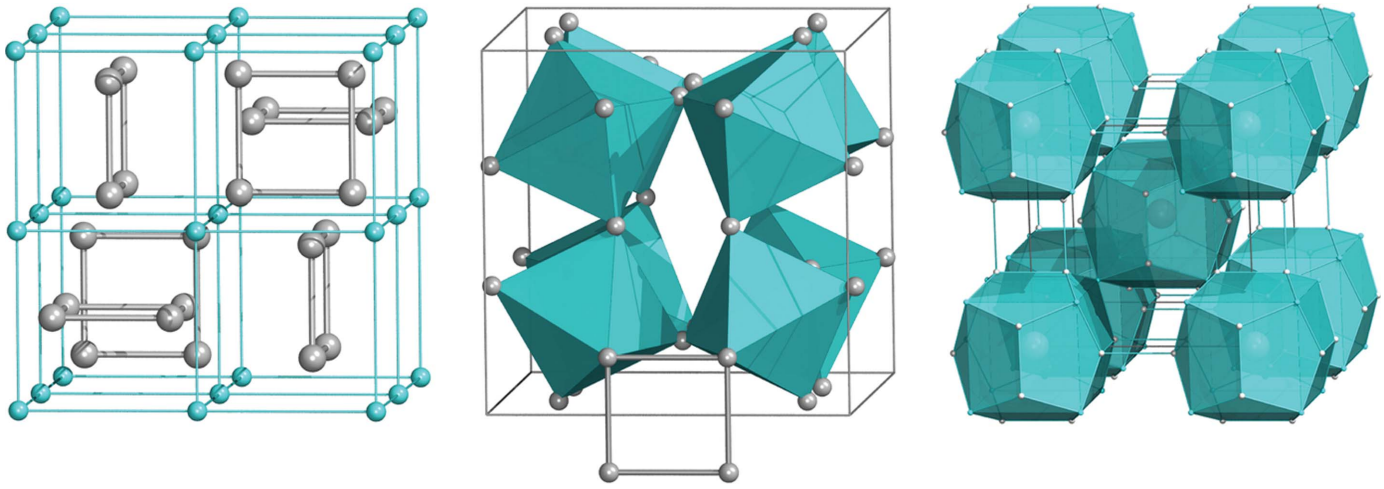

Figure 1
Structure of $CoSb_3$ depicting a cubic lattice of Co atoms with Sb_4 rings in six out of eight cube centres (left), the $CoSb_6$ octahedra and the Sb_4 unit (middle), and the cages linked by the long Sb—Sb bonds in the Sb_4 rings (right).

context, a number of challenges associated with experimental CD analysis of an inorganic, heavy-element and highly symmetric compound such as $CoSb_3$ were outlined. To summarize, particularly critical are the problems associated with extinction effects, since these can be quite severe and therefore difficult to correct for, in highly crystalline inorganic solids. The presence of heavy elements further complicates matters since the majority of the information on the diffuse valence electrons is contained within a few, potentially extinction-affected low-order reflections, and this makes compounds such as $CoSb_3$ unsuited for conventional X-ray diffraction studies (Zhurov *et al.*, 2011). Additionally, problems associated with accumulation of systematic errors on high-symmetry Wyckoff positions (Cruickshank & Rollett, 1953; Rees, 1976) are of importance in the current study. Systematic errors can originate from *e.g.* X-ray beam instability, theta-dependent absorption, (anisotropic) extinction, integration errors from profile-fitting procedures *etc.* (Iversen *et al.*, 1996, 1999; Zhurov *et al.*, 2008; Blake *et al.*, 2009).

There are several approaches to experimentally circumvent the highly problematic extinction effects of which γ-ray (Jauch & Reehuis, 2002, 2009), electron (Spence, 1993; Zuo *et al.*, 1999; Friis *et al.*, 2003) and synchrotron X-ray (Overgaard *et al.*, 1999, 2003) diffraction methods should be mentioned. Since convergent-beam electron diffraction (CBED) experiments on $CoSb_3$ turned out to be only partly successful (Saeterli *et al.*, 2011), and since γ-ray diffraction studies are very time consuming and require large-volume samples, our approach has been to attempt to reduce extinction effects through the combined use of small crystals and intense, high-energy synchrotron radiation.

In order to investigate the effects of using different X-ray sources and crystal sizes, we present here a comparative study of state-of-the-art single-crystal diffraction data from a conventional diffractometer (a Huber diffractometer equipped with a scintillation point detector) together with three different synchrotron-based experiments [two from the APS (Advanced Photon Source) using different CCD detectors and one from SPring8 using an image-plate detector (Sugimoto *et al.*, 2010)]. A comparison is also made with the powder synchrotron X-ray diffraction data used in the study of Ohno *et al.* (2007).

While $CoSb_3$ presents a strong challenge to the X-ray CD method, it is a favourable material for theoretical analysis. The high symmetry and semi-metallic properties make DFT calculations a well suited method, which in this case can serve as a benchmark. The subsequent analysis will show that one data set (SPring8) is by far the most accurate both in terms of R values and magnitudes of the residual density. This data set furthermore shows a favourable agreement with the theoretical data, confirming that experimental and theoretical structure factors serve as rigorous benchmarks for the quality of each other. With regard to chemical conclusions we refer to our communication that concerns detailed analysis of the CD derived from these data. Here we discuss the underlying key crystallographic analysis and conclusions for such studies in general.

2. Structure and bonding in $CoSb_3$

$CoSb_3$ crystallizes in the cubic space group $Im\bar{3}$ (Z = 8) with Co atoms in the corners of the cubic lattice interspersed with Sb_4 rings in six out of eight cubelets (Fig. 1, left). Both Co at $(\frac{1}{4}, \frac{1}{4}, \frac{1}{4})$ and Sb at $(0, y, z)$ occupy special Wyckoff positions in the unit cell. All Co–Sb interactions in the structure are equivalent, whereas there are two distinct Sb–Sb interactions resulting in two different interatomic Sb—Sb bond lengths. The $CoSb_3$ structure can also be described in terms of trigonally distorted corner-sharing $CoSb_6$ octahedra connected by the Sb_4 rings as illustrated in Fig. 1 (middle) (Papoian & Hoffmann, 2000; Lefebvre-Devos *et al.*, 2001). Based on the observation of comparable covalency in the Sb—Sb and Sb—Co bonds, Ohno *et al.* (2007) pointed out that the structure consists of large pentagonal dodecahedral cages linked by the longer Sb—Sb bonds and centred around the (0, 0, 0) site in

the unit cell (Fig. 1, right). The shorter Sb–Sb contacts form some of the edges in the cage, and Co—Sb bonds form the others.

Upon doping, guest atoms can enter into the cages, thereby lowering the thermal conductivity of the compound. For example, Kitagawa *et al.* (2000) examined the structural changes caused by filling Ce atoms into the cages of the $CoSb_3$ skutterudite structure. It was shown that the lattice constant increased and that the two different Sb–Sb distances approached each other. In line with this, Chakoumakos & Sales (2006) noted that in general the Pn_4 ring in skutterudites '*becomes squarer as the filling fraction increases*' and that, in the case of $CoSb_3$, it '*appears to become ideally square at 100% filling*'.

According to simple crystal-field theory, an octahedral field around a transition metal causes a splitting of the five 3*d*-electron levels into three degenerate t_{2g} and two e_g orbitals. Taking into account only electrostatic interactions, the e_g orbitals will be higher in energy than t_{2g} as the former are pointing towards the surrounding ligands. The Co atom resides at $(\frac{1}{4}, \frac{1}{4}, \frac{1}{4})$ which is characterized by $\bar{3}$ (C_{3i}) site symmetry. As a consequence, $CoSb_6$ moieties are not perfect octahedra and further splitting of Co *d* states occurs with respect to the standard t_{2g}/e_g separation in a perfectly octahedral O_h ligand field. However, for simplicity, we will adopt this latter simplified description in order to illustrate results from the literature. In addition, non-negligible covalent contributions to the interactions between Co and the surrounding Sb ligands are likely to further complicate the bonding picture (Anno *et al.*, 2000). The so-called Dudkin model for skutterudite compounds has been proposed (Dudkin, 1958) for the interaction of Co with the surrounding Sb ligands. In this picture Co atoms form bonds with the surrounding Sb atoms through the formation of d^2sp^3 hybrid orbitals. According to Anno *et al.* (2000) the Co(3*d*) orbitals with e_g symmetry hybridize with the Sb(5*p*) orbitals to form part of the conduction band and cause strong covalent interactions. The t_{2g} orbitals (located inside the valence band) are considered to be almost completely filled with a t_{2g}^6 configuration leading to the diamagnetic, semiconducting properties of the compound (Ackermann & Wold, 1977; Jung *et al.*, 1990; Sofo & Mahan, 1998; Anno *et al.*, 2000; Lefebvre-Devos *et al.*, 2001). This description seems to be supported by theoretical and experimental studies showing that the 3*d* states on Co hybridize with the 5*p* orbitals on the Sb ligand (Anno *et al.*, 2000; Lefebvre-Devos *et al.*, 2001; Ishii *et al.*, 2002; Koga *et al.*, 2005). The two Sb–Sb interactions are both expected to engage in 2*c*–2*e* covalent bonds (Ackermann & Wold, 1977; Grosvenor *et al.*, 2006). Lefebvre-Devos *et al.* (2001) concluded that the valence density of the highest band in the band structure is mainly situated in the $CoSb_6$ octahedra. They take this as an indication that the Co–Sb interactions are at least as important as the Sb—Sb bonds. They furthermore found that the short Sb–Sb interaction is stronger than the long Sb–Sb interaction and that the Co–Sb and Sb–Sb interactions are qualitatively similar. This is supported by the MEM study of Ohno *et al.* (2007). These findings have furthermore been confirmed in our published charge-density study of $CoSb_3$ based on the experimental data set that, judged from the comparison in the current study, is the most accurate (Schmøkel *et al.*, 2013). Based on topological analysis of the experimental and theoretical electron density (Bader, 1990), the Co–Sb and Sb–Sb interactions were concluded mainly to be of covalent character and the preferential filling of the t_{2g}-like states was clearly expressed in the Laplacian distribution. The atomic basin charges, of around −1/2 e for Co and +1/6 e for Sb, were found to be small in agreement with electronegativity values [Pauling: 1.88 for Co and 2.05 for Sb (Allred, 1961), Sanderson: 2.56 for Co and 2.46 for Sb (Sanderson, 1988)].

The atomic charges qualitatively agree with the findings of Ghosez & Veithen (2007) and Bertini & Cenedese (2007); based on periodic DFT calculations on $CoSb_3$ they obtained atomic basin charges for Co and Sb of, respectively, −0.53 e and +0.17 e (Ghosez), and −0.298 e and 0.093 e (Bertini). The result also agrees with the calculations of Koga *et al.* who determined the Co 3*d* population to about 7 e leading to a $t_{2g}^6 e_g^1$ configuration (Koga *et al.*, 2005). This compares well with the results from our published charge-density study which, based on the multipole populations, yielded a 3*d* population of ∼7 e (Schmøkel *et al.*, 2013). It is furthermore supported by the results from X-ray fluorescence experiments and band structure calculations by Kurmaev *et al.* (2004) that indicate an increase in the population of the 3*d* states on Co (to 7.36 e) in $CoSb_3$ compared to that of pure Co (∼7 e). However, it is in contradiction with the findings of Prytz *et al.* (2007), who report an emptying of the 3*d* shells ($\sim 3d^{8.0}$) with respect to elemental Co ($\sim 3d^{8.3}4s^{0.7}$) which they attribute to d^2sp^3 hybridization in accordance with the Dudkin model. It is also in opposition to Anno *et al.* (2000), who suggest a charge transfer from Co to Sb, as well as Grosvenor *et al.* (2006), who determine the atomic charges to be +3 e for Co and −1 *e* for Sb, leading to the often-assumed $t_{2g}^6 e_g^0$ configuration of the Co(3*d*) orbitals. Clearly, information about the atomic charges is important for considerations of host–guest interactions in doped thermoelectric materials.

3. Experimental details

3.1. Data collection

The refinements of four different experimental single-crystal X-ray diffraction data sets are compared; one is from a conventional in-house X-ray source collected at Aarhus University, and three are from the synchrotron sources at the APS in Chicago and SPring8 in Japan. Additionally, a comparison is made with results of the refinement against structure factors obtained from the powder X-ray diffraction data measured at SPring8. For further details on the latter we refer to the work by Ohno *et al.* (2007).

A single crystal of maximum dimension ∼120 µm was used for the data collection performed on the in-house X-ray source, and the same ∼10 µm crystal was used for the three synchrotron experiments. The two crystals are from the same batch grown by chemical vapour transport deposition with

Table 1
Crystallographic information on theoretical and experimental data sets on $CoSb_3$.

	Theory	SPring8	APS05	APS08	Aarhus	Powder
λ (Å)	N/A	0.4117	0.4133	0.4428	0.5608	0.42066
Size (μm)	N/A	10	10	10	120	N/A
T (K)	N/A	10 (1)	16 (1)	16 (1)	10.5 (5)	10
a, b, c (Å)	9.0209	9.0209 (3)	9.0285 (4)	9.0268 (1)	9.0173 (5)	9.016459 (1)
μ (mm^{-1})	N/A	5.27	5.31	6.46	12.72	N/A
Transmission	N/A	0.948665	0.948285	0.937442	0.217317	N/A
$\sin\theta/\lambda_{max}$	1.6100	1.6665	1.2677	1.6149	1.2337	1.8055
$N_{collected}$, N_{unique}	N/A, 2306	58020, 2559	16741, 1038	14310, 2317	33077, 1071	N/A, 3227
Redundancy	N/A	22.7	15.1	6.2	30.9	N/A
R_{int} (%)	N/A	3.8	4.3	4.6	3.2	N/A

chlorine gas as transport agent (Schmidt *et al.*, 1987; Christensen, 2007). Only very low temperatures (∼10 K) were used for all data collections in order to reduce systematic errors such as thermal diffuse scattering and anharmonicity, and to enhance the signal-to-noise ratio of the high-order reflections (Larsen, 1995; Iversen *et al.*, 1997; Lippmann & Schneider, 2000; Overgaard *et al.*, 1999; Macchi *et al.*, 2001). The data collection in Aarhus used a four-circle Huber diffractometer equipped with an Ag-sealed X-ray tube and a scintillation point detector. The data sets from APS were collected at the ChemMatCARS beamline with a Huber four-circle diffractometer and a Bruker R6000 CCD detector in one case (APS05) and a Bruker D8 diffractometer and an APEXII CCD detector in another (APS08). The SPring8 data are from the BL02B1 beamline equipped with a Huber four-circle diffractometer and a cylindrical image-plate detector. An overview of the experimental parameters can be found in Table 1. A detailed description of data reduction, data scaling *etc*. for the various data sets can be found in the supplementary material [in connection with this, see also Henriksen *et al.* (1986), Lehmann & Larsen (1974) and Wu *et al.* (2002)].[1] For details concerning the theoretical calculations, we refer to our communication Schmøkel *et al.* (2013).

4. Refinements

Both the Co and Sb atoms of the structure lie on special positions, restricting the number of variables in the multipole refinements. The aspherical atom models employ scattering factors derived from Slater-type orbital (STO) relativistic wavefunctions found in the *VM* data bank of the *XD2006* program package (Volkov *et al.*, 2006). All the symmetry-allowed multipole parameters up to the hexadecapole level are refined for each atom together with the atomic positions and the anisotropic displacement parameters (ADPs). Furthermore, an isotropic, type-1 extinction correction with a Lorentzian mosaic distribution is performed (Becker & Coppens, 1974) and the data are corrected for anomalous dispersion. For Co, only the seven 3*d* electrons are considered as valence electrons. The two 4*s* valence electrons are considered to be frozen and are treated as part of the core, unaffected by the chemical environment. One of the problems arising in connection with modelling of the Co(4*s*) electrons using experimental data is the fact that their main contribution to the scattered intensity lies in a few of the lowest-order reflections, which are also the part of the data most severely affected by extinction effects (Coppens, 1985; Farrugia *et al.*, 2003, 2009; Farrugia & Evans, 2005; Schmøkel *et al.*, 2012). Attempts to include the 4*s* electrons in the valence shell using various models with different combinations of radial functions and initial valence populations were tested for the SPring8 single-crystal data set and for the theoretical data set (see the supplementary material and Schmøkel *et al.*, 2013). However, no significant improvement of the fitting was found in terms of R values and residual density. Furthermore, it became clear from these refinements that the 3*d* valence population of cobalt in $CoSb_3$ is close to that of the isolated atom (7 e), irrespective of the treatment of the two 4*s* electrons. Similar results were obtained in a γ-ray diffraction study on ferromagnetic hexagonal cobalt (Jauch & Reehuis, 2009). In the case of Sb, both the two 5*s* and the three 5*p* electrons are treated as valence electrons, with the remainder being core electrons.

For heavy atoms very high data resolution is necessary to properly separate anharmonic effects from electron deformation effects (Iversen *et al.*, 1999). In the present case refinement of anharmonic Gram–Charlier parameters against the full SPring8 data set gave insignificant and vanishingly small parameters, and a harmonic description of the atomic vibrations was therefore deemed adequate for both Co and Sb.

4.1. Comparison of the experimental sets

A comparison is made between the results of the multipole refinements against the various experimental data sets. In order to make the basis of reference for the comparisons as equal as possible, the data sets have been reduced to the same resolution and, as far as possible, the same reflections are included in all cases. Only the equivalents of the *hkl* reflections in the APS05 data set are used from the other data sets. Furthermore, since the Aarhus data comprise the data set with the lowest resolution 'only' data up to 1.234 $Å^{-1}$ are used for each data set. Nevertheless, we also show results from refinements using all data for selected data sets.

[1] Supplementary material for this paper is available from the IUCr electronic archives (Reference: PC5032). Services for accessing this material are described at the back of the journal.

Table 2
κ values obtained from refinement using the reduced and the full theoretical data sets; $s = \sin\theta/\lambda$.

	Reduced data (N_{refl} = 1011, s_{max} = 1.23 Å^{-1})		All data (N_{refl} = 2263, s_{max} = 1.60 Å^{-1})	
Theory	κ	κ'	κ	κ'
Co	0.9915 (4)	0.946 (7)	0.9916 (3)	1.020 (3)
Sb	0.9784 (5)	0.800 (5)	0.9784 (5)	0.803 (3)

For consistency in the comparison of the data sets, the radial expansion/contraction coefficients, κ and κ', in the models of the experimental data refinements have been fixed at values derived from an unrestricted multipole modelling (UMM) of the theoretical structure factors. The radial κ and κ' coefficients allow for an expansion (values <1) or contraction (values >1) of the spherical and deformation atomic valence density, respectively, in the multipole refinement. In the UMM refinement all multipole and structural parameters are refined; however, in the case of the static theoretical data all positional parameters are kept fixed at the SPring8 geometry and the thermal parameters are all fixed to zero. The κ,κ'-restricted multipole model (hereafter KKRMM) is chosen for the experimental data refinements because it is impossible to refine the radial parameters and still obtain convergence for some of the data sets. Furthermore, using theoretical κ and κ' values has the advantage of reducing the correlation between the multipole and the positional and thermal parameters in the refinement (Abramov *et al.*, 1999; Volkov, Gatti *et al.*, 2000). Two different sets of κ values are used. One set is obtained from refinement of the *full* ($\sin\theta/\lambda \leq 1.6$ Å^{-1}) theoretical data set and this is used in the refinement of the *full* experimental data sets. Another set is obtained from refinement of the *reduced* theoretical data set and this is used in the refinement of the *reduced* experimental data sets. The κ values are tabulated in Table 2. As shall be discussed later, it turns out that the topologies, particularly the Laplacian, of the resulting electron densities are quite sensitive to the values used for the κ parameters in the valence regions of Sb. The sensitivity of the topology with respect to the radial functions is a well known problematic feature of the multipole model and speaks in favour of a κ-restricted model (Volkov, Abramov *et al.*, 2000; Volkov, Gatti *et al.*, 2000).

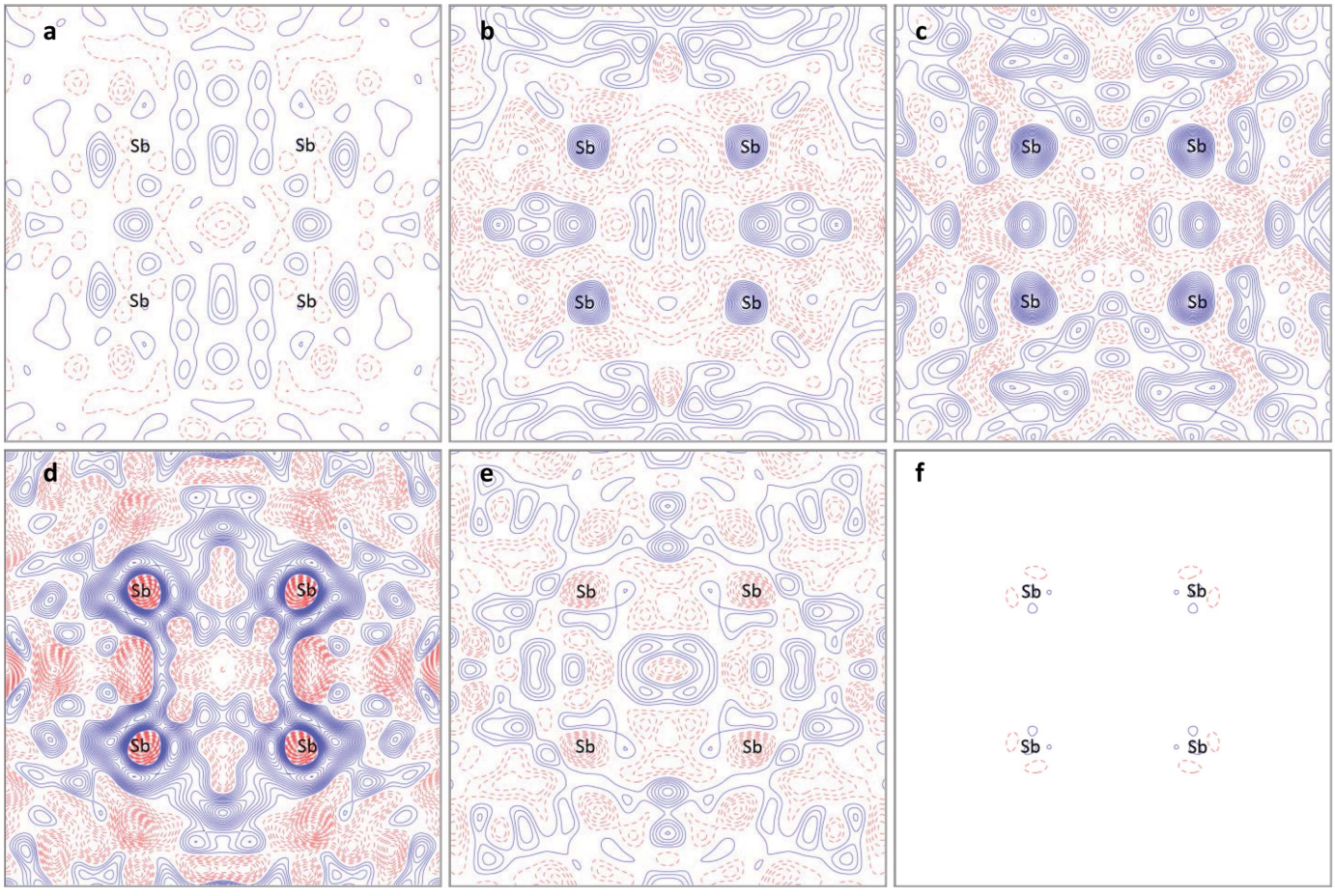

Figure 2
Residual density in the plane of the Sb_4 unit after multipole refinement against the reduced data sets: (*a*) SPring8, (*b*) APS05, (*c*) APS08, (*d*) Aarhus, (*e*) powder, (*f*) theory. Only reflections for which $\sin\theta/\lambda < 0.8$ Å^{-1} are included in the Fourier summation for the experimental data sets, whereas reflections up to 1.2337 Å^{-1} are included for the theoretical data set. The step size is 0.1 e Å^{-3} for the experimental data and 0.05 e Å^{-3} for the theoretical data. Full, blue contours are positive. Dashed, red contours are negative.

Table 3
Refinement results for the reduced experimental data sets.

	SPring8	APS05	APS08	Aarhus	Powder
$R(F^2)$	1.00%	2.30%	2.31%	3.39%	1.73%
GOF	0.981	1.350	1.255	3.610	0.827
$\pm\Delta\rho$ (e Å^{-3})	6.33/−1.51	7.93/−1.80	5.70/−1.15	12.02/−4.29	7.79/−2.77
$^{2nd}\Delta\rho_{max}$ (e Å^{-3})	1.47	2.21	2.64	4.33	2.82
$\pm\Delta\rho$ (e Å^{-3}) $s < 0.8$	1.89/−0.47	3.24/−0.64	2.67/−0.81	2.91/−2.03	1.79/−0.84
$^{2nd}\Delta\rho_{max}$ (e Å^{-3}) $s < 0.8$	0.48	1.17	1.58	1.73	0.64
$N_{refl\ input}$, $N_{refl\ used}$	1038, 989	1038, 891	1036, 994	1011, 987	1038, 923

The results of the refinements are shown in Table 3 and Fig. 2 for the reduced data sets, while the results from the full experimental data sets can be found in the supplementary material. In order to compare the models, the values of the highest and lowest residual density peaks are listed in the table. The highest positive value of the residual density is at the (0, 0, 0) site for all the experimental data sets. In the following we analyse three different explanations for this feature: (i) impurities in the sample; (ii) accumulation of errors at high-symmetry sites; (iii) an insufficient multipole model. Explanation (i) refers to the presence of a small amount of impurity Cl atoms included during the gas transport synthesis. However, this was ruled out based on EDX (energy-dispersive X-ray spectroscopy) experiments (see supplementary material). Furthermore, when investigating contour plots of the residual density at the (0, 0, 0) site (Fig. 3) the peak is much too narrow and sharp to portray a partly occupied guest atom in a large void. Thus, placing an atom (Cl or Co) at the cage-centre site in the model did not remove the residual entirely. It may also be noted that chemically it is unlikely that an anion (such as Cl^-) is present as a guest entity in a skutterudite structure. As shown below, the multipole model was expanded in many different ways without affecting the residual at this position, and the fact that the multipole model is an atom-centred model makes it very difficult to describe the residual at the origin using functions centred on the Co and Sb sites. For this reason we also rule out explanation (iii). Therefore, the large residual at the origin probably originates from error accumulation in this high-symmetry site [the (0, 0, 0) site has $m\bar{3}$ point symmetry] (Cruickshank & Rollett, 1953; Rees, 1976). The fact that the feature is always positive for

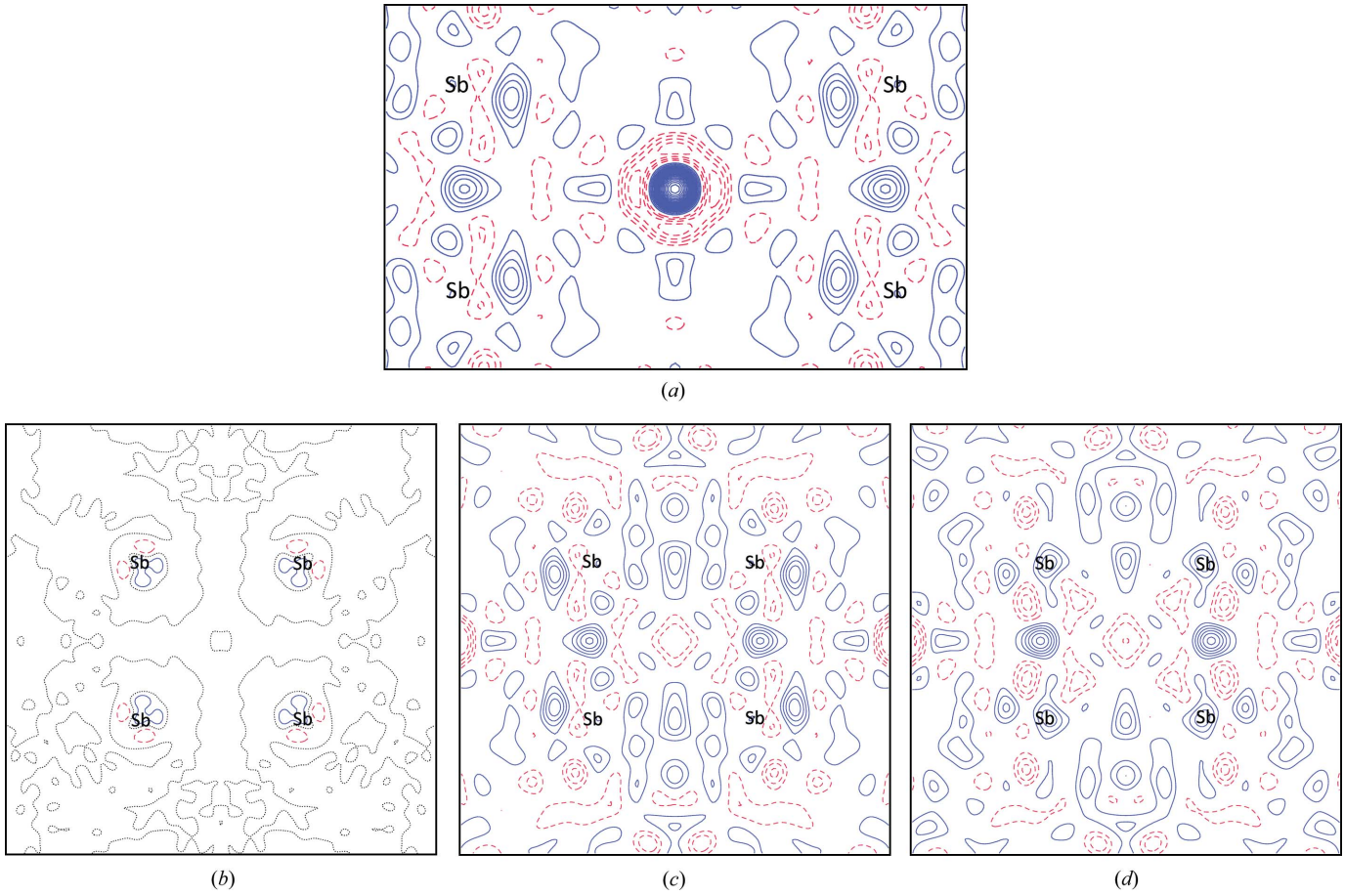

Figure 3
Residual densities after multipole modeling in (*a*) the 0, 0, 0 site for the full KKRMM fitted to SPring8 data, (*b*) the plane of the Sb_4 ring for the theoretical data, (*c*) the plane of the Sb_4 ring for the full KKRMM model fitted to SPring8 data, (*d*) the plane of the Sb_4 ring for the full UMM model fitted to SPring8 data. For theory all reflections are included and the step size is 0.05 e Å^{-3}. For the SPring8 data only reflections for which $\sin\theta/\lambda <$ 0.8 Å^{-1} are included and the contour step size is 0.1 e Å^{-3}. Full, blue contours are positive. Dashed, red contours are negative.

the experimental data sets could be an indication that it is due to some kind of systematic effect. It is possible that this feature will affect the final multipole model, but the fact that it is situated rather far (3.34 Å or more) from the atoms in the structure makes this unlikely and it will not be further discussed. One may also note that the excellent agreement between experiment and theory supports the fact that the effect is indeed minor. Instead, the second highest positive residual density peak will be considered in the following comparison of data quality. This peak is located either in the vicinity of the Sb atom or close to the centre of the Sb_4 ring. No systematic trends are observed for the positions of the negative residual density peaks. In most cases the minimum is found close to either the (0, 0, 0) site, the face-centre positions $(\frac{1}{2}, 0, \frac{1}{2})$ or along the (0, 0, z) line in the plane of the Sb_4 ring; *i.e.* at or close to high-symmetry sites in the unit cell, further verifying the significance of explanation (ii).

The residual density in the Sb_4 plane is plotted for $\sin\theta/\lambda < 0.8$ Å^{-1} in Fig. 2. The contour step size is 0.1 e Å^{-3} for the experimental data and 0.05 e Å^{-3} for the theoretical data. Equivalent plots for the full resolution of the data sets can be found in the supplementary material. Large differences are observed between the theoretical and experimental models for the nature and magnitude of the features shown in the plots. Comparing the experimental residual maps only, the residual density is clearly lower for the SPring8 data than all other experimental data sets. Residuals are found mainly in the regions of the Sb—Sb bonds in the former case; however, both the Sb—Sb midpoints lie at high-symmetry, low-multiplicity sites in the unit cell, which may be part of the explanation for the higher magnitude of the residual density in these regions. For the two APS data sets, the largest residuals are found at the positions of the Sb site and also in the Sb—Sb bonding region. In contrast, the Aarhus data show large negative values at the position of the Sb cores surrounded by a region of positive residual density. In general, the residual density values obtained from modelling of the conventional-source data are larger. Almost no residual density is found for the theoretical data in this plane, demonstrating that the multipole model can reproduce the data quite well. Introducing additional sets of multipolar functions for the core shells of each pseudoatom in order to describe any potential core polarization yielded an even better fit to the data (see the supplementary material).

Fig. 2 and Table 2 clearly show that the SPring8 data set is superior to the other experimental data sets in terms of both R values and magnitudes of the residual density. This may be due to the different details of the data-collection procedures as summarized in the following:

Redundancy. It is well established that in order to obtain accurate synchrotron diffraction data for which *e.g.* beam instability may be an issue, a high redundancy is necessary (Iversen *et al.*, 1999).

X-ray wavelength. This has an effect on the anomalous dispersion and the extinction parameters. As can be seen in Table 4 there is a clear correlation between both the wavelength and the crystal size with the extent of extinction. The crystal size has an equivalent effect on the degree of extinction; the smaller crystal shows the smallest effect.

Table 4
Wavelength, anomalous-dispersion parameters and the intensity reduction, x in % ($x = 1 - I_{\text{including extinction}}/I_{\text{extinction corrected}}$), due to extinction for the two most affected *hkl* reflections of the reduced data sets.

(130) is missing in the APS08 data set.

	SPring8	APS05	APS08	Aarhus
λ (Å)	0.4117	0.4133	0.4428	0.5608
f'(Co)	0.2152	0.2164	0.2378	0.3050
f'(Sb)	−3.6215	−3.3826	−2.0142	−1.0510
f''(Co)	0.3530	0.3556	0.4058	0.6330
f''(Sb)	0.5766	0.5808	0.6601	1.0146
μ (mm^{-1})	5.27	5.31	6.46	12.72
x(130)	0.5%	0.2%	N/A	49.0%
x(600)	0.2%	0.1%	16.1%	30.8%

Absorption and anomalous dispersion. Another competing effect related directly to the crystal size and the wavelength is the absorption of the X-ray beam within the crystal. The extent of absorption is determined by the linear absorption coefficient μ shown in Table 1. This effect is much larger for the Aarhus data due to the combined effect of the larger crystal and the longer wavelengths. Furthermore, the dispersion effects for cobalt are also larger for the in-house data than for the synchrotron data. However, when it comes to the dispersion effect related to f' for antimony, the picture is reversed. The effect is now the least for the long-wavelength data sets, since the synchrotron data were relatively close to the Sb K edge. The extent of the extinction and absorption effects on the in-house data is so high that a proper correction is practically impossible (Becker & Coppens, 1974). This diminishes the possibility of obtaining accurate intensity values and this is most probably the main reason for the difficulties encountered in the data fitting, leading to high R and residual density values for the in-house data set.

The CBED method of electron diffraction may, under good circumstances, measure accurate structure factors on an absolute scale and such a study was attempted for the $CoSb_3$ compound (Saeterli *et al.*, 2011). However, because of the relatively large unit cell only the F(200) and F(600) structure factors were successfully determined, resulting in absolute median values of 152.9 (4) and 665 (5), respectively. The F(200) value corroborates nicely with the SPring8 value of 153 (2), whereas the F(600) value of 649 (6) is slightly lower. A good agreement is observed with theory, for which F(200) = 154 and F(600) = 665, suggesting that CBED data may potentially be a useful contribution to this kind of study.

The clear conclusion from the comparison is that the synchrotron data sets provide the best results. When comparing the three synchrotron data sets to each other they still differ on some points. First of all, there might be differences in the performance of the sources, such as beam instability *etc.*, which are hard to quantify. Secondly, the redundancy is high for SPring8 and APS05, but low for APS08. However, the resolution for APS05 is low as opposed to APS08, meaning that the average redundancy is not directly comparable, as this will typically decrease with increasing

Table 5
Results from refinements of the theoretical data and the experimental SPring8 data with $\sin\theta/\lambda < 1.6$ Å^{-1}.

For the SPring8 data two refinements are made: one in which the κ, κ' values are refined (UMM) and one where they are fixed at the theoretical values (KKRMM). N_{refl} is the final number of reflections after application of the $I/\sigma(I)$ rejection criterion. For SPring8, the scale factor was refined and the refinement was based on F^2. For theory, the scale factor was kept fixed and the refinement was based on F.

		$I/\sigma(I) < 3$ rejected		No $I/\sigma(I)$ rejection	
	Theory (UMM)	SPring8 (KKRMM)	SPring8 (UMM)	SPring8 (KKRMM)	SPring8 (UMM)
$R(F^2)$	0.04%	1.27%	1.34%	1.37%	1.42%
N_{refl}	2263	1942	1942	2224	2224
$\pm\Delta\rho$ (e Å^{-3})	0.15/−0.16	7.85/−1.81	8.04/−1.78	6.46/−2.36	6.68/−2.50
$^{2nd}\pm\Delta\rho$ (e Å^{-3})	0.06/−0.09	2.41/−1.78	2.27/−1.69	2.78/−2.33	2.85/−2.33
$\pm\Delta\rho$ (e Å^{-3}) $\sin\theta/\lambda < 0.8$ Å^{-1}		1.86/−0.46	2.04/−0.44	1.83/−0.46	1.62/−0.48
$^{2nd}\Delta\rho_{max}$ (e Å^{-3}) $\sin\theta/\lambda < 0.8$ Å^{-1}		0.53	0.64	0.49	0.64
y (Sb)	0.33522	0.335221(4)	0.335221(4)	0.335221(4)	0.335221(4)
z (Sb)	0.15786	0.157861 (4)	0.157860 (4)	0.157861 (4)	0.157861 (4)
U_{11} (Sb)		0.00222 (1)	0.00221 (1)	0.00222 (1)	0.00220 (1)
U_{22} (Sb)		0.00266 (1)	0.00265 (1)	0.00266 (1)	0.00265 (1)
U_{33} (Sb)		0.00240 (1)	0.00239 (1)	0.00240 (1)	0.00239 (1)
U_{23} (Sb)		0.00010 (1)	0.00010 (1)	0.00010 (1)	0.00010 (1)
U_{11} (Co)		0.00248 (1)	0.00248 (1)	0.00248 (1)	0.00248 (1)
U_{12} (Co)		0.00005 (1)	0.00005 (1)	0.00005 (1)	0.00005 (1)
$P_{valence}$ (Co)	7.047 (4)	7.5 (1)	7.1 (2)	7.3 (1)	7.0 (2)
$P_{valence}$ (Sb)	4.984 (1)	4.85 (4)	4.97 (7)	4.88 (3)	5.00 (6)
κ, κ' (Co)	0.9916 (3), 1.020 (3)	0.991563, 1.019832	1.02 (1), 0.74 (7)	0.991563, 1.019832	1.02 (1), 0.74 (7)
κ, κ' (Sb)	0.9790 (4), 0.803 (3)	0.979001, 0.803150	1.09 (3), 0.69 (6)	0.979001, 0.803150	1.10 (3), 0.75 (6)

$\sin\theta/\lambda$. Only the SPring8 data have a very high redundancy in the entire resolution range. Furthermore, this data set has been collected with an image plate (Sugimoto *et al.*, 2010) whereas the APS data have been collected using a CCD detector. The higher dynamic range of the image plate (Zhurov *et al.*, 2008) makes it possible to more accurately measure the very intense low-order data, which must be well determined in order to properly obtain information about the valence density and the extinction in the crystal, while at the same time also collecting sufficiently significant weak reflections. It is possible that the problems related to the refinement of the radial valence density parameters, κ and κ', for many of the data sets originate from relatively poorly determined low-order data. This problem should not apply to the powder diffraction data to the same extent as single-crystal diffraction data. However, comparing R values and residual density peaks, the performance of the powder data is slightly worse than that of the single-crystal synchrotron data sets (Table 3 and Fig. 2). Despite the advantages of diminished extinction and absorption effects when collecting data on a powder sample, the single-crystal SPring8 data set seems superior.

Overall, the single-crystal SPring8 data are the best and, in order to evaluate their accuracy, they are compared to theoretical calculations in the following. Without the restrictions of having to study the common set of *hkl* values, for the remainder of the paper the full ($\sin\theta/\lambda \leq 1.6$ Å^{-1}) SPring8 and theoretical data sets are used.

5. Comparison of SPring8 data and theory

This section is related to our communication (Schmøkel *et al.*, 2013) concerning topological analysis of the CD of $CoSb_3$ obtained from the experimental SPring8 and the theoretical data, and it serves the purpose of making a detailed comparison between the density distributions obtained from two different ways of treating the radial parameters in the model applied to the experimental data.

The theoretical structure factors were modelled with a UMM where both the κ and κ' values were refined. The experimental SPring8 data set was modelled both with the UMM and the KKRMM, *i.e.* with κ and κ' values held fixed at the values determined by modelling of the theoretical data (Table 5). The aim of this comparison between these two models is to emphasize the sensitivity of heavy-element valence densities to the changes in the radial functions.

As seen from Fig. 3(*b*), the highest residuals for the theoretical data are found close to the centre of the atomic positions. This could be due to core expansion/contraction and core polarization effects as found recently for other systems (Fischer *et al.*, 2011; Overgaard *et al.*, 2011). Such features are not included in the model, which is based on a spherical neutral-atom core (results from a multipole model attempting to describe the residual density features at the core can be found in the supplementary material). However, the magnitude of the residual density for the theoretical data is generally much lower than found when modelling the experimental data. In the following analysis it will be shown that, in spite of the difficulties in the modelling of the experimental data, a qualitatively similar picture can be obtained for the resulting electron density obtained from theory and experiment.

Comparing the two multipole models of the experimental data, the lowest R value is obtained for the KKRMM model. Plots of the residual density in the Sb_4 plane can be found in Fig. 3. Clearly the two experimental models do not fully describe the electron density in the Sb—Sb bonding regions, even when neglecting the more noise-filled high-order data. However, as previously mentioned, part of the explanation for the higher magnitude of the residual density at the Sb—Sb

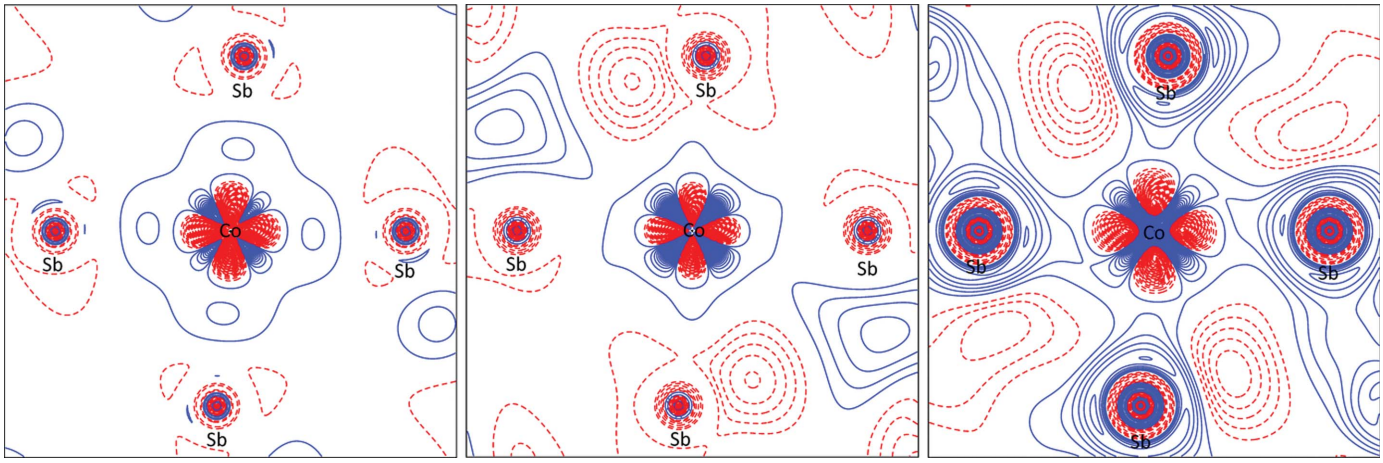

Figure 4
Contour plots of the static deformation density in the plane of the $CoSb_4$ unit for the theoretical data (left) and the SPring8 data fitted with the KKRMM model (middle) and the UMM model (right). The contour step size is 0.03 e Å^{-3}. Full, blue contours are positive. Dashed, red contours are negative.

midpoints may be related to noise accumulation at high-symmetry sites. The midpoint of the vertical Sb–Sb interaction intersects the (0, 0, z) line of special positions whereas the midpoint of the horizontal Sb—Sb bond intersects the ($\frac{1}{2}$, y, 0) line. There seem to be slightly larger problems in describing the short, vertical Sb–Sb interaction with the UMM compared with the KKRMM. For the former model positive residuals are found at the positions of the antimony atoms. This may be related to the small differences in valence populations and the difference in the κ, κ' parameters (Table 5).

Considering the static deformation density in the Sb_4 (Fig. S6 in the supplementary material) and the $CoSb_4$ (Fig. 4) planes, the same qualitative picture is obtained for the experimental and theoretical data. For the Sb_4 plane, charge is moved from the part of the antimony atoms pointing away from the Sb_4 ring to the Sb–Sb and Co–Sb interatomic regions when comparing the density from the multipole model to the density of the independent atom model (IAM). For both plots obtained from the SPring8 data, the positive peak of the deformation density seems to be displaced slightly outwards for the Sb–Sb interactions compared with theory. Apart from this, the plots obtained from theory and SPring8 KKRMM qualitatively agree, whereas for the SPring8 UMM deformation density additional positive features appear around the antimony atoms. This difference between the SPring8 KKRMM and UMM Sb densities can be assigned to the difference in the radial functions. In support of this, problems related to the determination of the radial parameters also lead to positive residual features surrounding antimony atoms in an experimental charge-density study of Sb_2O_3 (Whitten *et al.*, 2004). In the case of Co, the deformation density shows the expected features of maxima pointing towards the faces of the $CoSb_6$ octahedron and the minima pointing towards the six ligands (Stevens *et al.*, 1980) and there is only little difference between the three plots.

The same observations as those made from evaluation of the static deformation density are found when performing a topological analysis (Bader, 1990) of the three electron-density distributions. These are compared in Fig. 5, where atomic graphs with bond critical points (black dots) and valence shell charge concentration (VSCC) non-bonded maxima (red dots) are shown. Bond critical points (b.c.p.'s) are found directly on or very near the straight line connecting Co and Sb for both theory and experiment. However, the Sb_4 unit exhibits differences in the b.c.p. positions for theory and experiment, resulting in bond paths between Sb atoms that are curved outwards for the experimental densities, while for theory the Sb—Sb bond paths are almost straight lines. The feature is more pronounced for the vertical, short Sb–Sb interaction as expected from the contour plot of the static deformation density (Fig. S6). For the experimental KKRMM density an unexpected (3, −3) critical point is found in the topology of the Laplacian near the Sb atom which is not present in the other two cases. However, a closer inspection of

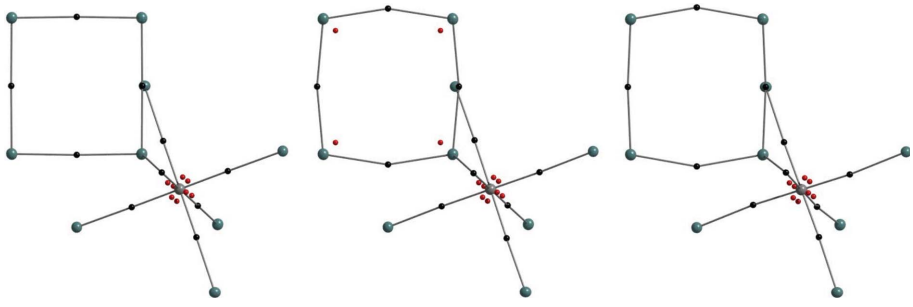

Figure 5
Atomic graphs for the $CoSb_6$ octahedra and the Sb_4 rings showing the bond critical points (black dots) and the (3, −3) critical points in the negative Laplacian distribution, $-\nabla^2\rho$, corresponding to the maxima in the VSCC (red dots). The plots are viewed along the [$\bar{1}$00] direction, *i.e.* along the $-a$ axis of the unit cell. Left: theoretical density. Middle: experimental KKRMM density. Right: experimental UMM density.

Table 6
Topological analysis of the bond critical points (b.c.p.'s) for the Co–Sb and Sb–Sb interactions in $CoSb_3$ based on multipole-fitted densities and on the theoretical density derived directly from the wavefunction (*WIEN2k*).

The *TOPXD* (Volkov, Abramov *et al.*, 2000) and *XDPROP* programs of the *XD2006* package have been used for the calculations on the multipole-modelled densities. Uncertainties on the interatomic distances, *d*, are at the fifth decimal place. The errors reported for density, $\rho_{b.c.p.}$, and the Laplacian, $\nabla^2\rho_{b.c.p.}$, are obtained from the *XDPROP* module of the *XD2006* program package. The random errors obtained from the least-squares fitting are unrealistically small as seen *e.g.* in the larger change of $\rho_{b.c.p.}$ and $\nabla^2\rho_{b.c.p.}$ values when slightly changing the radial model. AIL: atomic interaction line. $H_{b.c.p.}$: total energy density.

		d (Å)	AIL_{Sb-X} (Å)	$AIL_{Sb-b.c.p.}$ (Å)	$\rho_{b.c.p.}$ (e Å^{-3})	$\nabla^2\rho_{b.c.p.}$ (e Å^{-5})	$H_{b.c.p.}$ (a.u.)
Sb—Sb long	SPring8 KKRMM	2.973	2.986	1.493	0.33 (3)	0.21 (3)	−0.018
	SPring8 UMM	2.973	2.976	1.488	0.39 (2)	−0.08 (2)	−0.025
	Theory, multipole	2.973	2.973	1.486	0.316	0.33	−0.016
	Theory, *WIEN2k*	2.973	2.973	1.486	0.334	−0.12	−0.020
Sb—Sb short	SPring8 KKRMM	2.848	2.884	1.442	0.40 (2)	0.20 (3)	−0.025
	SPring8 UMM	2.848	2.902	1.451	0.37 (2)	0.66 (2)	−0.020
	Theory, multipole	2.848	2.848	1.424	0.378	0.17	−0.023
	Theory, *WIEN2k*	2.848	2.848	1.424	0.393	−0.25	−0.026
Co—Sb	SPring8 KKRMM	2.523	2.524	1.331	0.395 (8)	1.71 (1)	−0.019
	SPring8 UMM	2.523	2.529	1.371	0.421 (7)	1.47 (1)	−0.023
	Theory, multipole	2.529	2.524	1.343	0.426	1.54	−0.023
	Theory, *WIEN2k*	2.523	2.523	1.355	0.426	1.22	−0.025

the curvatures of this point reveals that the Laplacian distribution is very flat in two directions compared to the third ($|\lambda_2| \sim 10$, $|\lambda_3| \sim 0$, $|\lambda_1| \sim 10^6$), and this indicates that this critical point is not trustworthy.

The values of the topological descriptors evaluated at the Co—Sb and Sb—Sb b.c.p.'s are reported in Table 6, both for the densities obtained from multipole refinement and for the theoretical density derived directly from the wavefunction in *WIEN2k* (Blaha *et al.*, 2008). When comparing the theoretical density obtained from multipole refinement against theoretical structure factors (multipole) with that directly obtained from the wavefunction (*WIEN2k*), the major discrepancies are found for the values of the Laplacian at the Sb—Sb b.c.p.'s. It is well known (Volkov, Abramov *et al.*, 2000) that multipole refinement of theoretical structure factors introduces a bias in the theoretical electron density and its derivatives compared with the direct density. The cause of this has mainly been attributed to the limited flexibility of the single-zeta radial functions employed in the multipole model (Volkov, Abramov *et al.*, 2000; Volkov & Coppens, 2001). In line with this, the agreement between the topology of experimental and theoretical densities has been shown to improve '*when the theoretical densities are projected into the multipole model through refinement of the theoretical structure factors*' (Volkov, Abramov *et al.*, 2000). Therefore, the focus is placed on the topologies of the multipole refined electron densities.

The topology of the electron density obtained from the KKRMM fitting of the SPring8 data matches the topology of the multipole-fitted theoretical electron density quite well. The only measure in Table 6 which indicates a significant difference is the Laplacian at the b.c.p.'s. The differences in the Laplacian for the Sb–Sb interactions are illustrated by the contour plots of the Laplacian for the Sb_4 unit in Fig. 6. From this it seems that the picture of bonding obtained from the density associated with the UMM fitting of the experimental electron density is different from the theoretical and the KKRMM density. Theory (multipole) and the KKRMM density indicate charge depletion at the position of the b.c.p.,

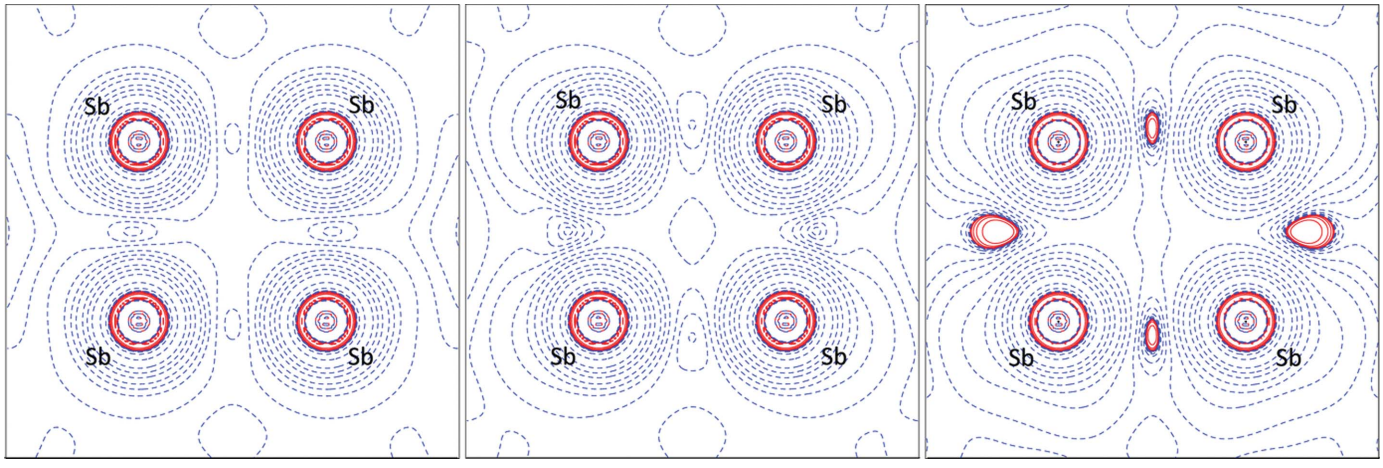

Figure 6
Contour plot of the Laplacian in the plane of the Sb_4 unit for the theoretical multipole fitted data (left), the KKRMM-fitted experimental data (middle) and the UMM-fitted experimental data (right). Positive contours are plotted with blue, dashed lines; negative contours with full, red lines.

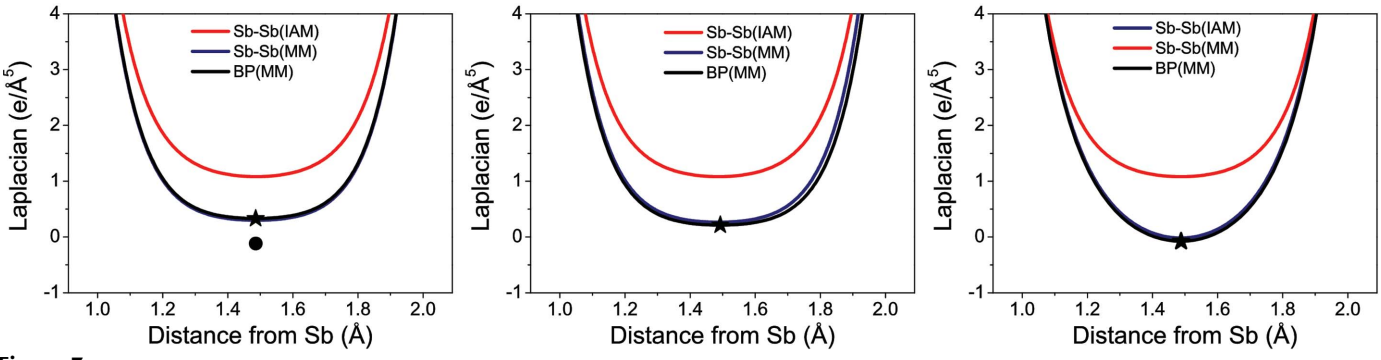

Figure 7
The Laplacian plotted along the direction of the long Sb–Sb interaction for the theoretical data (left), the experimental KKRMM model (middle) and the experimental UMM model (right). The black and blue lines are the multipole density along the bond path and the straight line connecting the atoms, respectively, and the red line is the IAM density. Stars mark the position of the b.c.p. and the circle marks the position of the b.c.p. for the direct theoretical density (*WIEN2k*).

while theory (*WIEN2k*, Table 6) and UMM indicate charge accumulation. However, it has previously been documented that care should be taken when interpreting the value of the Laplacian at the b.c.p. for interactions between heavy elements (Shi & Boyd, 1988; Gatti, 2005; Eickerling & Reiher, 2008). This is due to the loss of the correspondence between the Laplacian and the shell structure for the outer valence regions of the atoms involved. Because of this, the values of $\nabla^2\rho_{\rm b.c.p.}$ found for all types of bonds in Table 6 cannot be taken as a sign of the nature (ionic or covalent) of the interactions.

In order to assess whether the amount of charge accumulation in the bonding region is decreasing or increasing compared with a spherical, non-bonded reference density, the profile of the Laplacian is plotted along the line joining the various atoms for both the multipole and the IAM densities for the long Sb–Sb interactions in Fig. 7 and for the remaining bonds in the supplementary material. For both Co—Sb and Sb—Sb bonds, the same qualitative picture is obtained of increased charge accumulation between the pairs of atoms in the density resulting from multipole refinement. Only the profiles of the short Sb–Sb interaction for the UMM-fitted SPring8 data do not indicate additional charge accumulation compared with the IAM. The reason for this is most likely that the profile is evaluated for the straight line joining the atomic nuclei whereas the atomic interaction line (AIL), or bond path (BP), is not entirely straight in this case. The covalent character, indicated by relative charge accumulation in the true density, of all the bonds is confirmed by the negative value of the total energy density, $H_{\rm b.c.p.}$ (Table 6).

Comparing the three electron densities and their topologies, there seems to be a greater similarity between theory and SPring8 KKRMM compared to SPring8 UMM. This is a clear indication of the importance and sensitivity of the radial functions for the valence density. Nonetheless, overall the same qualitative picture is obtained from all three densities and for all three bond types. Thus, the emerging picture shows relatively low values of the density at the b.c.p.'s (ranging from 0.33 to 0.43 e Å^{-3}), but still an indication of a relative charge accumulation and enhanced shared interaction with respect to the IAM based on the static deformation density, the Laplacian profile and the negative values of the total energy density for all three interactions in $CoSb_3$.

6. Conclusion

Four low-temperature single-crystal X-ray diffraction data sets have been collected at different sources using different experimental conditions. The results clearly show that in the current study the data obtained from synchrotron sources were superior to data obtained from a conventional X-ray source. The requirements, when dealing with heavy-element compounds, are that the data need to be collected on a high-intensity, high-energy source using very small crystals in order to reduce extinction and absorption effects. Furthermore, the data need to be highly redundant far out in reciprocal space so that a high accuracy of the merged reflections is obtained. The data set collected at SPring8 fulfils these requirements most satisfactorily and it even performs slightly better than synchrotron powder diffraction data, for which the effects of absorption and extinction are vanishing.

For $CoSb_3$ it is difficult to acquire experimental data that are accurate enough in order for the radial parameters governing the expansion and contraction of the valence shells to be properly determined. It is found that a more reliable fit to the data was obtained by fixing these parameters at the values obtained from the theoretical data based on DFT calculations. In this case, a good agreement is found between the SPring8 and the theoretical data as reflected in the similarity of the topological properties.

This work was supported by the Danish National Research Foundation (Center for Materials Crystallography, DNRF93) and the Danish Research Council for Nature and Universe (Danscatt). The synchrotron radiation experiment at the SPring8 synchrotron was conducted with the approval of the Japan Synchrotron Radiation Research Institute. ChemMatCARS Sector 15 is principally supported by the National Science Foundation/Department of Energy under grant No. NSF/CHE-0822838. Use of the Advanced Photon Source was

supported by the US Department of Energy, Office of Science, Office of Basic Energy Sciences, under Contract No. DE-AC02-06CH11357.

References

Abramov, Y., Volkov, A. & Coppens, P. (1999). *Chem. Phys. Lett.* **311**, 81–86.

Ackermann, J. & Wold, A. (1977). *J. Phys. Chem. Solids*, **38**, 1013–1016.

Allred, A. (1961). *J. Inorg. Nucl. Chem.* **17**, 215–221.

Anno, H., Matsubara, K., Caillat, T. & Fleurial, J. (2000). *Phys. Rev. B*, **62**, 10737–10743.

Anno, H., Matsubara, K., Notohara, Y., Sakakibara, T. & Tashiro, H. (1999). *J. Appl. Phys.* **86**, 3780–3786.

Bader, R. F. W. (1990). *Atoms in Molecules: a Quantum Theory.* Oxford, New York: Oxford University Press.

Becker, P. J. & Coppens, P. (1974). *Acta Cryst.* A**30**, 129–147.

Bertini, L. & Cenedese, S. (2007). *Phys. Status Solidi (RRL)*, **1**, 244–246.

Bertini, L. & Gatti, C. (2004). *J. Chem. Phys.* **121**, 8983–8989.

Blaha, P., Schwarz, K., Madsen, G., Kvasnicka, D. & Luitz, J. (2008). *WIEN2k*. Technische Universität Wien, Austria.

Blake, A. J., Clegg, W., Cole, J. M., Evans, J. S. O., Main, P., Parsons, S. & Watkin, D. J. (2009). *Crystal Structure Analysis: Principles and Practice*, 2nd ed. Oxford University Press.

Caillat, T., Borshchevsky, A. & Fleurial, J. (1996). *J. Appl. Phys.* **80**, 4442–4449.

Chakoumakos, B. & Sales, B. (2006). *J. Alloys Compd.* **407**, 87–93.

Christensen, M. (2007). PhD thesis, Aarhus University, Aarhus, Denmark.

Coppens, P. (1985). *Coord. Chem. Rev.* **65**, 285–307.

Cruickshank, D. W. J. & Rollett, J. S. (1953). *Acta Cryst.* **6**, 705–707.

Dudkin, L. D. (1958). *Sov. Phys.-Tech. Phys.* **3**, 216–220.

Eickerling, G. & Reiher, M. (2008). *J. Chem. Theory Comput.* **4**, 286–296.

Farrugia, L. J. & Evans, C. (2005). *J. Phys. Chem. A*, **109**, 8834–8848.

Farrugia, L. J., Evans, C., Lentz, D. & Roemer, M. (2009). *J. Am. Chem. Soc.* **131**, 1251–1268.

Farrugia, L. J., Mallinson, P. R. & Stewart, B. (2003). *Acta Cryst.* B**59**, 234–247.

Fischer, A., Tiana, D., Scherer, W., Batke, K., Eickerling, G., Svendsen, H., Bindzus, N. & Iversen, B. B. (2011). *J. Phys. Chem.* **115**, 13061–13071.

Friis, J., Madsen, G. K. H., Larsen, F. K., Jiang, B., Spence, J., Marthinsen, K. & Holmestad, R. (2003). *J. Chem. Phys.* **119**, 11359–11366.

Gatti, C. (2005). *Z. Kristallogr.* **220**, 399–457.

Ghosez, P. & Veithen, M. (2007). *J. Phys. Condens. Matter*, **19**, 096002.

Grosvenor, A., Cavell, R. & Mar, A. (2006). *Phys. Rev. B*, **74**, 125102.

Henriksen, K., Larsen, F. K. & Rasmussen, S. E. (1986). *J. Appl. Cryst.* **19**, 390–394.

Ishii, H., Okazaki, K., Fujimori, A., Nagamoto, Y., Koyanagi, T. & Sofo, J. O. (2002). *J. Phys. Soc. Jpn*, **71**, 2271–2275.

Iversen, B. B., Larsen, F. K., Figgis, B. N. & Reynolds, P. A. (1997). *J. Chem. Soc. Dalton Trans*. pp. 2227–2240.

Iversen, B. B., Larsen, F. K., Figgis, B. N., Reynolds, P. A. & Schultz, A. J. (1996). *Acta Cryst.* B**52**, 923–931.

Iversen, B. B., Larsen, F. K., Pinkerton, A. A., Martin, A., Darovsky, A. & Reynolds, P. A. (1999). *Acta Cryst.* B**55**, 363–374.

Jauch, W. & Reehuis, M. (2002). *Phys. Rev. B*, **65**, 125111.

Jauch, W. & Reehuis, M. (2009). *Phys. Rev. B*, **80**, 125126.

Jung, D., Whangbo, M. H. & Alvarez, S. (1990). *Inorg. Chem.* **29**, 2252–2255.

Kitagawa, H., Hasaka, M., Morimura, T., Nakashima, H. & Kondo, S. (2000). *Mater. Res. Bull.* **35**, 185–192.

Koga, K., Akai, K., Oshiro, K. & Matsuura, M. (2005). *Phys. Rev. B*, **71**, 155119.

Kurmaev, E. Z., Moewes, A., Shein, I. R., Finkelstein, L. D., Ivanovskii, A. L. & Anno, H. (2004). *J. Phys. Condens. Matter*, **16**, 979–987.

Larsen, F. K. (1995). *Acta Cryst.* B**51**, 468–482.

Lefebvre-Devos, I., Lassalle, M., Wallart, X., Olivier-Fourcade, J., Monconduit, L. & Jumas, J. (2001). *Phys. Rev. B*, **63**, 125110.

Lehmann, M. S. & Larsen, F. K. (1974). *Acta Cryst.* A**30**, 580–584.

Lippmann, T. & Schneider, J. R. (2000). *J. Appl. Cryst.* **33**, 156–167.

Macchi, P., Larsen, F. K., Schultz, A. & Iversen, B. B. (2001). *J. Phys. Chem. A*, **105**, 9231–9242.

Mi, J., Christensen, M., Nishibori, E. & Iversen, B. B. (2011). *Phys. Rev. B*, **84**, 064114.

Mi, J., Christensen, M., Nishibori, E., Kuznetsov, V., Rowe, D. M. & Iversen, B. B. (2010). *J. Appl. Phys.* **107**, 113507.

Morelli, D., Caillat, T., Fleurial, J., Borshchevsky, A., Vandersande, J., Chen, B. & Uher, C. (1995). *Phys. Rev. B*, **51**, 9622–9628.

Nolas, G. S., Morelli, D. T. & Tritt, T. M. (1999). *Annu. Rev. Mater. Sci.* **29**, 89–116.

Nolas, G. S., Slack, G. A., Caillat, T. & Meisner, G. P. (1996). *J. Appl. Phys.* **79**, 2622–2626.

Ohno, A., Sasaki, S., Nishibori, E., Aoyagi, S., Sakata, M. & Iversen, B. (2007). *Phys. Rev. B*, **76**, 064119.

Overgaard, J., Jones, C., Dange, D. & Platts, J. A. (2011). *Inorg. Chem.* **50**, 8418–8426.

Overgaard, J., Larsen, F. K., Schiøtt, B. & Iversen, B. B. (2003). *J. Am. Chem. Soc.* **125**, 11088–11099.

Overgaard, J., Schiøtt, B., Larsen, F. K., Schultz, A. J., MacDonald, J. C. & Iversen, B. B. (1999). *Angew. Chem. Int. Ed.* **38**, 1239–1242.

Papoian, G. A. & Hoffmann, R. (2000). *Angew. Chem. Int. Ed.* **39**, 2409–2448.

Prytz, Ø., Taftø, J., Ahn, C. & Fultz, B. (2007). *Phys. Rev. B*, **75**, 125109.

Rees, B. (1976). *Acta Cryst.* A**32**, 483–488.

Saeterli, R., Flage-Larsen, E., Friis, J., Løvvik, O. M., Pacaud, J., Marthinsen, K. & Holmestad, R. (2011). *Ultramicroscopy*, **111**, 847–853.

Sales, B. C., Mandrus, D. & Williams, R. K. (1996). *Science*, **272**, 1325–1328.

Sanderson, R. T. (1988). *J. Chem. Educ.* **65**, 112–118.

Schmidt, Th., Kliche, G. & Lutz, H. D. (1987). *Acta Cryst.* C**43**, 1678–1679.

Schmøkel, M. S., Bjerg, L., Overgaard, J., Krebs Larsen, F., Hellerup Madsen, G. K., Sugimoto, K., Takata, M. & Brummerstedt Iversen, B. (2013). *Angew. Chem. Int. Ed.* **52**, 1503–1506.

Schmøkel, M. S., Cenedese, S., Overgaard, J., Jørgensen, M. R., Chen, Y. S., Gatti, C., Stalke, D. & Iversen, B. B. (2012). *Inorg. Chem.* **51**, 8607–8616.

Shi, Z. & Boyd, R. J. (1988). *J. Chem. Phys.* **88**, 4375–4377.

Singh, D. & Pickett, W. (1994). *Phys. Rev. B*, **50**, 11235–11238.

Sofo, J. & Mahan, G. (1998). *Phys. Rev. B*, **58**, 15620–15623.

Spence, J. C. H. (1993). *Acta Cryst.* A**49**, 231–260.

Stevens, E. D., DeLucia, M. L. & Coppens, P. (1980). *Inorg. Chem.* **19**, 813–820.

Sugimoto, K., Ohsumi, H., Aoyagi, S., Nishibori, E., Moriyoshi, C., Kuroiwa, Y., Sawa, H. & Takata, M. (2010). *AIN Conf. Proc.* **1234**, 887–890.

Volkov, A., Abramov, Y., Coppens, P. & Gatti, C. (2000). *Acta Cryst.* A**56**, 332–339.

Volkov, A. & Coppens, P. (2001). *Acta Cryst.* A**57**, 395–405.

Volkov, A., Gatti, C., Abramov, Y. & Coppens, P. (2000). *Acta Cryst.* A**56**, 252–258.

Volkov, A., Macchi, P., Farrugia, L. J., Gatti, C., Mallinson, P., Richter, T. & Koritsanszky, T. (2006). *XD2006. A Computer Program Package for Multipole Refinement, Topological Analysis of*

Charge Densities and Evaluation of Intermolecular Energies from Experimental or Theoretical Structure Factors. University at Buffalo, State University of New York, NY, USA; University of Milano, Italy; University of Glasgow, UK; CNR-ISTM, Milano, Italy; Middle Tennessee State University, TN, USA.

Whitten, A. E., Dittrich, B., Spackman, M. A., Turner, P. & Brown, T. C. (2004). *Dalton Trans.* pp. 23–29.

Wu, G., Rodrigues, B. L. & Coppens, P. (2002). *J. Appl. Cryst.* **35**, 356–359.

Zhurov, V. V., Zhurova, E. A. & Pinkerton, A. A. (2008). *J. Appl. Cryst.* **41**, 340–349.

Zhurov, V. V., Zhurova, E. A., Stash, A. I. & Pinkerton, A. A. (2011). *J. Phys. Chem. A*, **115**, 13016–13023.

Zuo, J. M., Kim, M., O'Keeffe, M. & Spence, J. C. H. (1999). *Nature (London)*, **401**, 49–52.